PHYSICAL REVIEW E **93**, 033113 (2016)

Lattice Boltzmann simulation of three-dimensional Rayleigh-Taylor instability

H. Liang,[1] Q. X. Li,[2] B. C. Shi,[3,4] and Z. H. Chai[3,4,*]
[1]*Department of Physics, Hangzhou Dianzi University - Hangzhou 310018, China*
[2]*Department of Urban and Rural Planning, Zhejiang University of Finance and Economics - Hangzhou 310018, China*
[3]*School of Mathematics and Statistics, Huazhong University of Science and Technology, Wuhan 430074, China*
[4]*State Key Laboratory of Coal Combustion, Huazhong University of Science and Technology, Wuhan 430074, China*

(Received 7 November 2015; revised manuscript received 13 January 2016; published 14 March 2016)

In this paper, the three-dimensional (3D) Rayleigh-Taylor instability (RTI) with low Atwood number ($A_t = 0.15$) in a long square duct ($12W \times W \times W$) is studied by using a multiple-relaxation-time lattice Boltzmann (LB) multiphase model. The effect of the Reynolds number on the interfacial dynamics and bubble and spike amplitudes at late time is investigated in detail. The numerical results show that at sufficiently large Reynolds numbers, a sequence of stages in the 3D immiscible RTI can be observed, which includes the linear growth, terminal velocity growth, reacceleration, and chaotic development stages. At late stage, the RTI induces a very complicated topology structure of the interface, and an abundance of dissociative drops are also observed in the system. The bubble and spike velocities at late stage are unstable and their values have exceeded the predictions of the potential flow theory [V. N. Goncharov, Phys. Rev. Lett. **88**, 134502 (2002)]. The acceleration of the bubble front is also measured and it is found that the normalized acceleration at late time fluctuates around a constant value of 0.16. When the Reynolds number is reduced to small values, some later stages cannot be reached sequentially. The interface becomes relatively smoothed and the bubble velocity at late time is approximate to a constant value, which coincides with the results of the extended Layzer model [S.-I. Sohn, Phys. Rev. E **80**, 055302(R) (2009)] and the modified potential theory [R. Banerjee, L. Mandal, S. Roy, M. Khan, and M. R. Guptae, Phys. Plasmas **18**, 022109 (2011)]. In our simulations, the Graphics Processing Unit (GPU) parallel computing is also used to relieve the massive computational cost.

DOI: 10.1103/PhysRevE.93.033113

I. INTRODUCTION

Rayleigh-Taylor instability (RTI) is a very classical and fundamental interfacial instability, which will occur at the perturbed interface between fluids of different densities in the presence of gravity force. This instability plays a significant role in diverse areas such as astrophysics [1], geophysics [2], and confinement fusion [3]. Due to its wide and important applications, the RTI has been extensively studied. The earliest study of the RTI can be traced back to the theoretical analysis by Rayleigh and Taylor [4]. Through their analysis, they developed the linear stability theory and showed that the disturbance is unstable when its initial amplitude is much smaller than its wavelength. They further found that the amplitude of the disturbance has an exponential growth with time and the linear growth rate can be expressed as a function of the density ratio. In their analysis, however, the fluids are supposed to be inviscid and the surface tension force is absent. The addition of the viscosity, surface tension force, or compressibility in the linear theory was conducted in the subsequent studies [5–9].

The first experimental study on the RTI was attributed to Lewis [10], who validated the classical linear stability theory [4] with experiment, and qualitatively described the development stages of the RTI. Later, Sharp [11] further investigated the RTI qualitatively and roughly divided the growth of the instability into four stages. For the first stage, the linear stability theory can be applied to describe the interface movement until the amplitude of the initial perturbation grows to 0.1λ–0.4λ, where λ is the wavelength. Subsequently, the perturbation develops nonlinearly, and the heavy fluid and the light one penetrate into each other in the form of the spike and bubble, which indicates that the RTI has entered into the second stage. The third stage is characterized by the increasing nonlinear effect. The heavy fluid rolls up along the flank of the spike and forms into the mushroom-like structure, which is caused by the Kelvin-Helmholtz (KH) instability providing the rolling motion of the interface. The roll-up phenomenon is more pronounced at low-density ratios. Finally, the spike breaks up and the turbulent or chaotic mixing of the fluids dominates the fourth stage of the RTI.

Following Lewis' work [10], numerous researchers have conducted experimental studies on the RTI with the single-mode [12–16] or multimode [17–19] initial perturbations. The study of the single-mode RTI is still important not only in its own interests, but also in the fact that the turbulent growth constant in the multimode instability depends critically on the knowledge of single-mode terminal velocity [20]. Waddell *et al.* [13] experimentally investigated the two-dimensional (2D) single-mode RTI in the low Atwood number fluid systems. The experimental results showed that the disturbance on the interface grows with an exponential form at an early stage and the measured growth rate was shown to agree well with the linear stability theory. Additionally, they found that the average of the bubble and spike velocities at a late time closes to be constant. Wilkinson *et al.* [14] experimentally studied the three-dimensional (3D) single-mode RTI with a low Atwood number and observed that the instability at the late time exhibits an acceleration. Both the bubble and spike were accelerated to the corresponding velocities above the classical model values [21,22]. This disagreement is ascribed

---

[*] hustczh@126.com

to the formation of vortices on the bubble-spike interface [23]. It should be stressed that in the experimental studies on the single-mode RTI [12–16], the duration of the instability evolution is relatively short ($H_b \leqslant 1.5\lambda$, where H_b is the amplitude of the bubble), although they claimed to investigate the late-time RTI [24]. The long-time experiments are still difficult due to the size limitations of the facilities. Besides, it is also challenging to accurately measure the large interfacial topology change and related physical quantities at late time.

With the rapid development of the computational technology, numerical simulation becomes an important complement to experimental studies and many researchers have made an effort to simulate the single-mode RTI [23–37], while most of these works are only to validate the developed CFD methods, and the evolution time is very short ($H_b \leqslant \lambda$). Glimm *et al.* [33] used the front tracking approach to perform longer simulations ($H_b \approx 2\lambda$) of 2D single-mode RTI with moderate Atwood numbers. They reported a new phenomena of the RTI that the instability undergoes a reacceleration stage after the plateau time. The reacceleration stage was also observed in the later 3D simulations by Ramaprabhu *et al.* [23] and experiments by Wilkinson *et al.* [14]. Recently, Ramaprabhu *et al.* [35] further numerically investigated the late time behavior ($H_b \approx 3.5\lambda$) of 3D single-mode RTI with two miscible fluids. Their results showed that the reacceleration cannot last continuously and the instability at late time is translated into the chaotic mixing stage. In this stage, the spike and bubble velocities seems to show a decrease lower than the potential flow velocity at high Reynolds numbers, which is in contradiction with the result of a high-resolution direct numerical simulation of 2D single-mode RTI that the bubble has a mean quadratic growth at late time [24]. This late-time quadratic growth phenomenon was also observed in our 2D simulations with an improved lattice Boltzmann model [37].

As shown above, there have been some numerical works to investigate the late-time single-mode RTI [24,35,37]. However, most of these [24,37] focus on only the 2D phenomenon and 3D immiscible RTI at late time is still not well understood. To fill this gap, in this paper a lattice Boltzmann (LB) multiphase model based on the advanced multiple-relaxation-time (MRT) collision operator is employed to study the late-time dynamics of 3D RTI. The effect of the Reynolds number on the interfacial behaviors and bubble and spike velocities is fully investigated. To our knowledge, the durations of the instability in our simulations ($H_b \approx 5.5\lambda$) is longer than those of the previous study [35] and a different picture of the late-time RTI will be presented here. The rest of this paper is organized as follows. In Sec. II, we gives a brief introduction of the adopted LB multiphase model. The computational results are presented in Sec. III, where the long-time evolution of 3D instability at high Reynolds numbers is first examined. Finally, we made a summary in Sec. IV.

II. NUMERICAL METHOD

The LB method, which is based on mesoscopic kinetic equations, has received great success in modeling multiphase flows [38]. Currently, from different physical pictures, several types of LB multiphase models have been proposed, which mainly include the color-gradient model [39], the pseudo-potential model [40], the free-energy model [41], and the phase-field based models [30,37,42–45]. The last class of LB models is based on the phase-field theory [46], which has become increasingly popular since the interface physics in this theory can be well described. We recently developed a new phase-field-based LB model for simulating 2D multiphase flows [37], which is able to significantly improve the accuracy and stability in the interface tracking. In addition, the MRT collision model is used in Ref. [37] to improve the numerical stability. The MRT model can degenerate to the single-relaxation-time (SRT) or so-called Bhatnagar-Gross-Krook model if the relaxation matrix is diagonal. Due to the more free adjustable relaxation parameters, the MRT model has its superiority over the SRT model in terms of numerical stability and accuracy [47,48,55]. In particular, it has been shown that the MRT model retains a better numerical stability in studying the low-viscosity or high-Reynolds-number multiphase flows [37,49]. Later, this model is also extended to study the 3D [50] and axisymmetric [51] multiphase flows. In this work, the 3D LB model based on the MRT collision operator will be invoked to investigate the late-time dynamics of the instability.

For completeness, we quickly recall the 3D LB model. This model utilizes two LB equations, one of which is used to track the interface and the other is adopted to derive the fluid velocity and pressure. The LB equation with the MRT collision model for the interface tracking can be written as

$$\begin{aligned} f_i(\mathbf{x}+\mathbf{e}_i\delta_x,t+\delta_t) - f_i(\mathbf{x},t) \\ = -(\mathbf{M}^{-1}\mathbf{S}\mathbf{M})_{ij}\left[f_j(\mathbf{x},t) - f_j^{\mathrm{eq}}(\mathbf{x},t)\right] + \delta_t F_i(\mathbf{x},t), \end{aligned} \quad (1)$$

where $f_i(\mathbf{x},t)$ is the order distribution function and $f_i^{\mathrm{eq}}(\mathbf{x},t)$ is the equilibrium distribution function, which takes the linear form [37]

$$f_i^{\mathrm{eq}}(\mathbf{x},t) = \begin{cases} \phi + (\omega_i - 1)\eta\mu, & i = 0, \\ \omega_i\eta\mu + 4\omega_i\phi\mathbf{e}_i\cdot\mathbf{u}, & i \neq 0, \end{cases} \quad (2)$$

where ϕ is the order parameter, μ is the chemical potential, and is a function of ϕ [52]:

$$\mu = 4\beta\phi(\phi-1)(\phi+1) - k\nabla^2\phi, \quad (3)$$

where the parameters β and k depend on the interface thickness D and surface tension σ by the relationships $k = 3D\sigma/8$ and $\beta = 3\sigma/4D$. $\mathbf{e}_i$ and ω_i in Eq. (2) represent the lattice velocity and the weighting coefficient, which are determined by the discrete-velocity model. Here the three-dimensional seven-velocity (D3Q7) model is used for simplicity and high computational efficiency. In this model, $\mathbf{e}_i$ and ω_i can be given as

$$\mathbf{e}_i = \begin{bmatrix} 0 & 1 & -1 & 0 & 0 & 0 & 0 \\ 0 & 0 & 0 & 1 & -1 & 0 & 0 \\ 0 & 0 & 0 & 0 & 0 & 1 & -1 \end{bmatrix}, \quad (4)$$

$$\omega_0 = \tfrac{1}{4}, \quad \omega_{1-6} = \tfrac{1}{8}. \quad (5)$$

The corresponding collision matrix $\mathbf{M}$ for the D3Q7 model can be found in Refs. [50,53]. To derive the Cahn-Hilliard equation correctly, the source term in Eq. (1) is defined by

$$F_i = \left[\mathbf{M}^{-1}\left(\mathbf{I} - \frac{\mathbf{S}}{2}\right)\mathbf{M}\right]_{ij} \frac{4\omega_j \mathbf{e}_j \cdot \partial_t \phi \mathbf{u}}{c}, \tag{6}$$

where $\mathbf{I}$ is the 7×7 unit matrix and $\mathbf{S}$ is the diagonal matrix with $\mathbf{S} = \text{diag}\ (1,s_1,s_1,s_1,s_2,s_3,s_3)$. In our model, the order parameter can be computed by

$$\phi = \sum_i f_i, \tag{7}$$

and the local density is obtained from

$$\rho = \frac{1+\phi}{2}\rho_l + \frac{1-\phi}{2}\rho_g, \tag{8}$$

where ρ_l and ρ_g denote the densities of liquid and gas phases. Using the Chapman-Enskog expansion for the D3Q7 model, Eq. (1) can result in the Cahn-Hilliard equation in the incompressible limit,

$$\frac{\partial \phi}{\partial t} + \nabla \cdot (\phi \mathbf{u}) = \nabla \cdot (M \nabla \mu), \tag{9}$$

where M is the mobility given by $M = \frac{\eta}{4}(\frac{1}{s_1} - 0.5)\delta x$.

The fluid velocity and pressure are derive from the density distribution function g_i. Following Refs. [37,54], the MRT LB equation with the forcing term for g_i is given by

$$\begin{aligned} g_i(\mathbf{x} + \mathbf{e}_i\delta_x, t + \delta_t) - g_i(\mathbf{x},t) \\ = -(\Lambda^{-1}\mathbf{T}\Lambda)_{ij}\left[g_j(\mathbf{x},t) - g_j^{\text{eq}}(\mathbf{x},t)\right] \\ + \delta_t\left[\Lambda^{-1}\left(\mathbf{I} - \frac{\mathbf{T}}{2}\right)\Lambda\right]_{ij} G_j, \end{aligned} \tag{10}$$

where g_i^{eq} is the equilibrium distribution function of g_i,

$$g_i^{\text{eq}} = \begin{cases} \frac{p}{c_s^2}(\omega_i - 1) + \rho s_i(\mathbf{u}), & i = 0, \\ \frac{p}{c_s^2}\omega_i + \rho s_i(\mathbf{u}), & i \neq 0, \end{cases} \tag{11}$$

where $s_i(\mathbf{u})$ is denoted as

$$s_i(\mathbf{u}) = \omega_i\left[\frac{\mathbf{e}_i \cdot \mathbf{u}}{c_s^2} + \frac{(\mathbf{e}_i \cdot \mathbf{u})^2}{2c_s^4} - \frac{\mathbf{u} \cdot \mathbf{u}}{2c_s^2}\right], \tag{12}$$

where $c_s = \sqrt{1/3}$. For the three-dimensional 15-velocity (D3Q15) model adopted in this work, the weight coefficients ω_i and the discrete velocities $\mathbf{e}_i$ in Eqs. (11) and (12) can be presented as

$$\mathbf{e}_i = \begin{bmatrix} 0 & 1 & -1 & 0 & 0 & 0 & 0 & 1 & -1 & 1 & -1 & 1 & -1 & 1 & -1 \\ 0 & 0 & 0 & 1 & -1 & 0 & 0 & 1 & 1 & -1 & -1 & 1 & 1 & -1 & -1 \\ 0 & 0 & 0 & 0 & 0 & 1 & -1 & 1 & 1 & 1 & 1 & -1 & -1 & -1 & -1 \end{bmatrix}, \tag{13}$$

$$\omega_0 = \tfrac{2}{9}, \quad \omega_{1-6} = \tfrac{1}{9}, \quad \omega_{7-14} = \tfrac{1}{72}. \tag{14}$$

The transformation matrix Λ of the D3Q15 model can be referred to Ref. [55]. $\mathbf{I}$ in Eq. (10) is the 15×15 unit matrix and $\mathbf{T}$ is the diagonal relaxation matrix denoted by $\mathbf{T} = \text{diag}(1,\lambda_1,\lambda_2,1,\lambda_3,1,\lambda_3,1,\lambda_3,\lambda_4,\lambda_4,\lambda_4,\lambda_4,\lambda_4,\lambda_5)$. The total forces including the interfacial tension force and external body force need to be implemented in the LB algorithm. To recover the exact Navier-Stokes equations, the forcing term G_i in Eq. (10) is given by

$$G_i = \frac{(\mathbf{e}_i - \mathbf{u})}{c_s^2} \cdot \left[s_i(\mathbf{u})\nabla\left(\rho c_s^2\right) + (\mathbf{F}_s + \mathbf{F}_a + \mathbf{G})(s_i(\mathbf{u}) + \omega_i)\right], \tag{15}$$

where $\mathbf{F}_s = \mu\nabla\phi$ is the surface tension force, $\mathbf{F}_a = 0.5(\rho_l - \rho_g)M\nabla^2\mu\mathbf{u}$ is an additional interfacial force [56], $\mathbf{G}$ is the gravitational force. To incorporate these force effects, the macroscopic pressure and velocity can be computed by

$$\mathbf{u} = \frac{\sum_i \mathbf{e}_i g_i + 0.5\delta_t(\mathbf{F}_s + \mathbf{G})}{\rho - 0.25(\rho_l - \rho_g)M\nabla^2\mu}, \tag{16}$$

$$p = \frac{c_s^2}{(1 - \omega_0)}\left[\sum_{i\neq 0} g_i + \frac{\delta_t}{2}\mathbf{u} \cdot \nabla\rho + \rho s_0(\mathbf{u})\right]. \tag{17}$$

Through the Chapman-Enskog multiscale analysis, Eq. (10) can be reduced to the Navier-Stokes equations under the incompressible condition, and the resulting equations are

$$\nabla \cdot \mathbf{u} = 0, \tag{18a}$$

$$\rho\left(\frac{\partial \mathbf{u}}{\partial t} + \mathbf{u} \cdot \nabla\mathbf{u}\right) = -\nabla p + \nabla \cdot [\nu\rho(\nabla\mathbf{u} + \nabla\mathbf{u}^T)] + \mathbf{F}_s + \mathbf{G}, \tag{18b}$$

where $\nu = c_s^2(\frac{1}{\lambda_4} - 0.5)\delta_t$.

In the implementation of the model, the time and spatial derivatives need to be evaluated numerically. To reduce the discretization errors, the following difference schemes are used [57,58]:

$$\partial_t\chi(\mathbf{x},t) = \frac{\chi(\mathbf{x},t) - \chi(\mathbf{x},t - \delta_t)}{\delta_t} \tag{19}$$

and

$$\nabla\chi(\mathbf{x},t) = \sum_{i\neq 0} \frac{\omega_i \mathbf{e}_i \chi(\mathbf{x} + \mathbf{e}_i\delta_t, t)}{c_s^2\delta_t}, \tag{20}$$

$$\nabla^2\chi(\mathbf{x},t) = \sum_{i\neq 0} \frac{2\omega_i[\chi(\mathbf{x} + \mathbf{e}_i\delta_t, t) - \chi(\mathbf{x},t)]}{c_s^2\delta_t^2}, \tag{21}$$

where χ is the arbitrary variable.

At the end of this section, we would like to point out that all simulations in this study are performed on the GPU machine, which is composed of a NVIDIA's K20 device. As we know, the implementation of LB algorithm only involves the local and neighbor nodes, so it is suitable for parallel computation. When it is carried out on the GPU platform, the computational efficiency can be greatly improved. The numerical experiments show that there is a considerable time saving, compared with a single CPU for simulating the same case.

III. RESULTS AND DISCUSSIONS

A. LB simulation results

The physical problem considered in this work is a rectangular box with an aspect ratio of $12W \times W \times W$, where W is the box width. Initially, an imposed square-mode perturbation with the wavelength W is imposed at the midplane ($z = 6W$),

$$h(x,y) = 0.05W[\cos(kx) + \cos(ky)], \tag{22}$$

where $k = 2\pi/W$ is the wave number. To be smooth across the interface, the initial order distribution $\phi(x,y,z)$ is given by

$$\phi(x,y,z) = \tanh 2\left[\frac{z - h(x,y) - 6W}{D}\right]. \tag{23}$$

The dimensionless Reynolds number (Re) and the Atwood number (A_t) are used to describe the RTI, and are defined by

$$\mathrm{Re} = \frac{W\sqrt{gW}}{\nu}, \quad A_t = \frac{\rho_l - \rho_g}{\rho_l + \rho_g}, \tag{24}$$

where g is a gravitational acceleration. We also define the dimensionless velocities of the bubble and spike fronts, which are commonly referred to the bubble and spike Froude numbers in the literature [23],

$$\mathrm{Fr}_b = \frac{u_b}{\sqrt{\frac{A_t gW}{1+A_t}}}, \quad \mathrm{Fr}_s = \frac{u_s}{\sqrt{\frac{A_t gW}{1+A_t}}}, \tag{25}$$

where u_b and u_s are the bubble and spike speeds. In our simulations, the densities of the liquid (ρ_l) and gas (ρ_g) are set to be 1.0 and 0.74, corresponding to a low A_t of 0.15 [14]. The physical parameters are fixed as $W = 100$, $\sqrt{gW} = 0.04$, $\sigma = 10^{-4}$, $D = 4$. The relaxation factors in the matrix $\mathbf{S}$ are given as $s_1 = 1.25$, $s_2 = 1.2$, $s_3 = 1$, and the parameters in the $\mathbf{T}$ are set to 1 [59], except for the λ_4 determined by the value of Re. The periodic boundary conditions are used in the lateral directions and the no-slip boundary conditions are applied at the upper and lower walls. To incorporate the gravitational effect, the following body force $\mathbf{G}$ in the z-direction is imposed to the fluids:

$$\mathbf{G} = \left[0,0,-\left(\rho - \frac{\rho_l + \rho_g}{2}\right)g\right]. \tag{26}$$

Figure 1 depicts the time evolution of the density contour in the immiscible RTI with four typical values of Re, where time is normalized by the characteristic time $1/\sqrt{A_t gk}$. It can be seen from Fig. 1 that under the influence of gravity, the heavy fluid first falls down and the light fluid rises up for all the cases. That is to say, the heavy and light fluids penetrate into each other at early time and the penetration length increases with time, which then leads to the formations of the spike and bubble. The spike and bubble continue to move in the opposite directions, while the KH instability arising from the differential velocity across the interface begins to develop, and its intensity increases as time advances. With the action of the KH instability, the spike rolls up and a mushroom-like structure appears [see time 5.8 in Fig. 1(a)–1(c)]. It is found that a similar pattern is also observed in some previous works [23,26,31], although the Reynolds numbers they considered are smaller than those in our studies. We also observe from Fig. 1 that the roll-up extent is reduced and the time is postponed with the decrease of Re. Particularly, the roll-up phenomenon dose not take place at low Re and the heavy fluid falls down freely in the form of the spike [see Fig. 1(d)], which can be attributed to the large viscosity effect that the frictional force between the bubble and spike is large and the KH instability providing the rolling motion of the interface is suppressed. In the following evolution time, the instability exhibits significantly distinct behaviors at various Reynolds numbers. At high Re, the spike continues to fall down, accompanied by the shrink of the roll-ups. The surface on them also becomes rough and four long curls emerge at the tails of the roll-ups [see time 9.7 in Fig. 1(a)], which is caused by large shear interaction between fluids. At last, the system is unstable. The interfaces undergo a dramatic deformation at the multiple layers and some of them even have a chaotic breakup, which induces the formation of numerous small dissociative drops in the system. In contrast, at low Re the structure of the interface becomes relatively smoothed and no breakup case can be found in the whole evolution processes.

To observe the evolution of the interface more clearly, we also plotted the interface patterns at the diagonal vertical plane (x = y) with above Reynolds numbers in Fig. 2. It is shown that for all the Reynolds numbers, the initial development of the mode follows the pattern familiar from 2D studies [13,24,30,37]. In the following, the distinct behaviors of the interface can be observed at different values of Re. For the high-Re case, the interface rolls up at the spike tip and the saddle point. Then two pairs of counter-rotating vortices are formed [see time 6.2 in Fig. 2(a)]. The two-layer roll-up phenomenon is a unique feature of 3D RTI, which is significantly different from that in the 2D situation. This phenomenon is also observed in the simulations with moderate Reynolds numbers, as shown in Figs. 2(b) and 2(c). However, the roll-ups appear at later time and the vortex sizes are substantially smaller as Re is decreased. For a typical case, we cannot find any vortex pattern at a low Re of 10. After time 6.2, the vortices develop further and become much longer, forming into two pairs of long curls. These curls squeeze the light fluid radially inward and then are in touch with the middle heavy fluid [see time 9.3 in Fig. 2(a)]. At this time, the nonlinear effect is very strong. Under the action of strong shear forces, the interface undergoes a large deformation including the multiple-layer roll-ups, which results in the formation of many small secondary vortices. These vortices are unstable and some of them break up, which contributes to the chaotic mixing of two fluids. Finally, a complex topology structure of the interface is formed at time 15.1. It is noted from Fig. 2(a) that the interface patterns preserve the symmetry at all evolution time, which are consistent with the results of high-resolution direct numerical simulations of 2D single-mode RTI [24]. These results also indicate that the LB

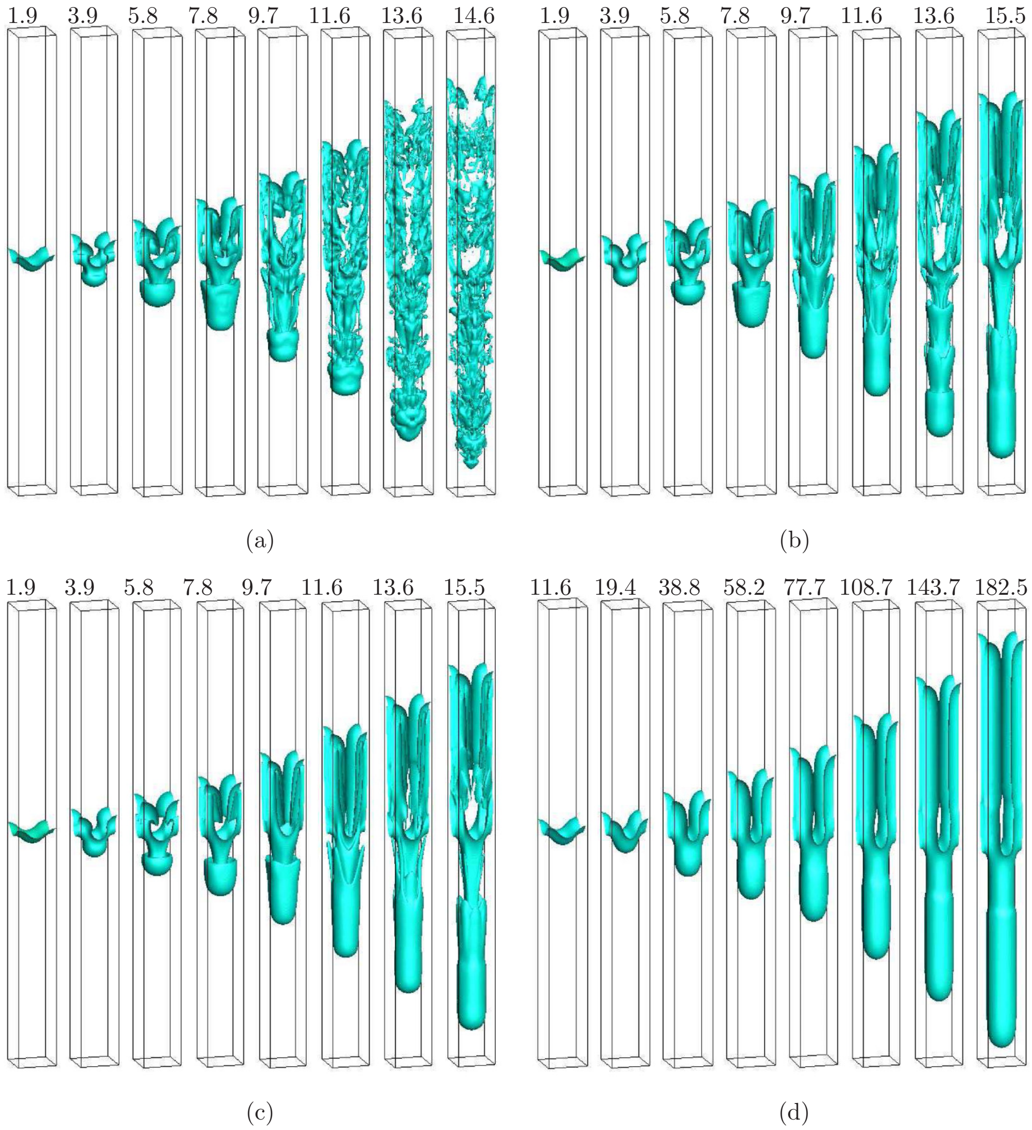

(a) (b)

(c) (d)

FIG. 1. Evolution of the density contours in immiscible RTI at various values of Re, (a) Re = 5000, (b) Re = 1000, (c) Re = 500, and (d) Re = 10. The time is normalized by the characteristic time $1/\sqrt{A_t g k}$.

method has a good accuracy in capturing small-scale structures of late-time RTI. Ramaprabhu *et al.* [35] also conducted simulations of 3D single-mode RTI using other numerical methods. They reported that the instability does not preserve the flow symmetry at late time, which is in contradiction with the present result. This inconsistency may be caused by the limitation of small-scale resolution or the adopted numerical methods [24]. For the low-Re case, the interface shows much simpler and more smoothed structure. It does not break up any more since the shear layer between the bubble and spike is stabilized at a larger viscosity.

As shown above, we have examined the effect of Re on the interfacial dynamics in 3D immiscible RTI. To further show its effect, we also conducted a quantitative measure on the amplitudes and velocities of the bubble and spike at various Reynolds numbers. The bubble and spike amplitudes and their evolution velocities are important physical quantities in 3D RTI, and have been extensively studied in the literatures [14,26,31]. However, these previous studies only focus on early stage of the evolution, and the Reynolds numbers considered are relatively small. Therefore it is desirable to investigate the late-time evolution of these physical quantities, especially at a large Re. If not specified, the amplitudes of the bubble and spike are denoted by H_b and H_s, which are defined as the vertical distances between the bubble and spike fronts and their corresponding initial positions. Figures 3(a) and 3(b) present the evolution of the normalized bubble amplitude and velocity at four typical Reynolds numbers. From Fig. 3(a), it is seen that the bubble amplitude increases with time for all Reynolds numbers, while it has a greater value at a larger Re. From Fig. 3(b), we identified the distinct growth stages as describing the velocity of the bubble tip at different Reynolds numbers. For high-Re case (Re = 5000), the RTI undergoes a complex sequence of stages, including linear growth, terminal velocity growth, reacceleration, and chaotic development. At the linear stage ($t \leqslant 2$), the disturbance is found to grow with

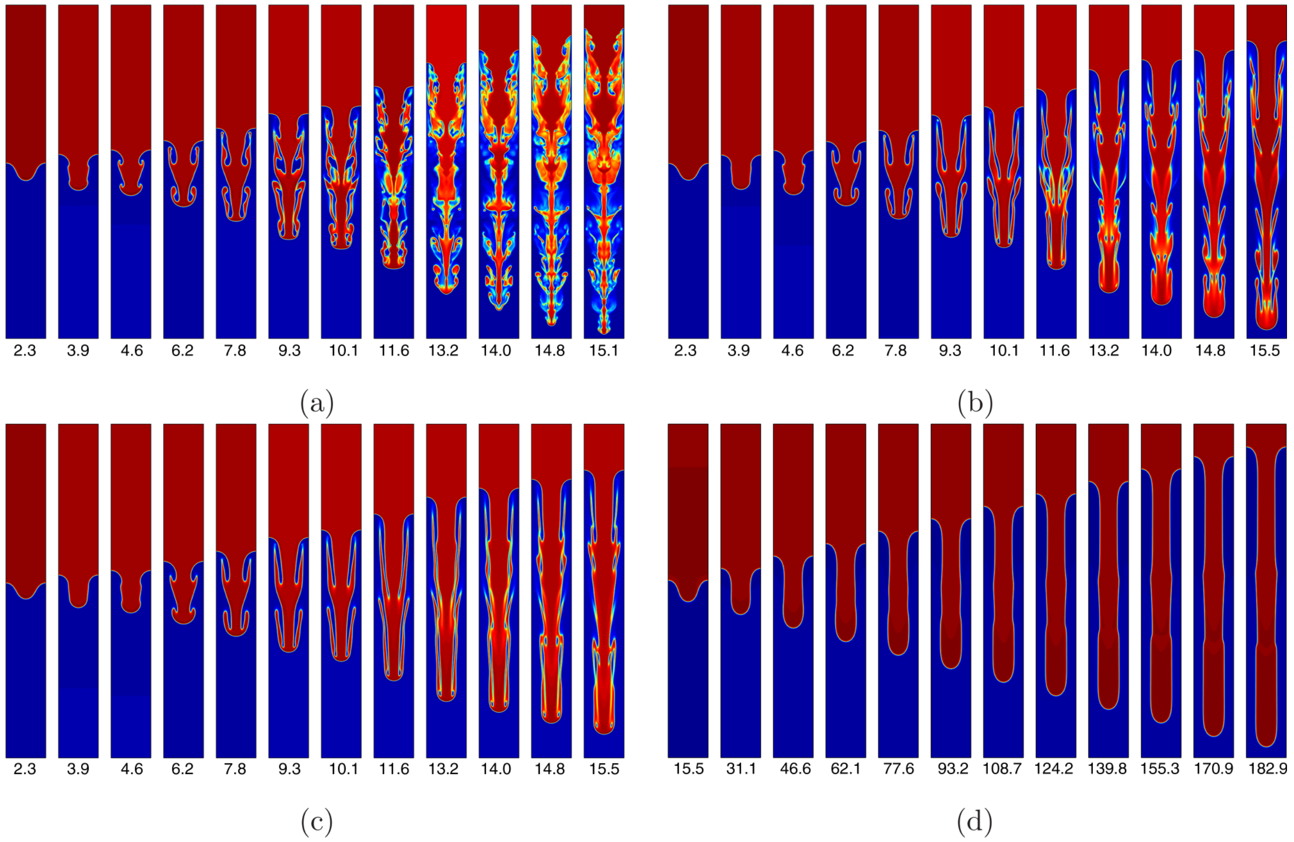

FIG. 2. Evolution of the density contour at the diagonal vertical plane ($x = y$): (a) Re = 5000, (b) Re = 1000, (c) Re = 500, and (d) Re = 10. The time is normalized by the characteristic time $1/\sqrt{A_t g k}$.

an exponential form [13,14],

$$h = a_1 e^{\gamma t} + a_2 e^{-\gamma t}, \tag{27}$$

where $h = \frac{h_b + h_s}{2}$ is the averaged amplitude of the bubble and spike, h_b and h_s represent the vertical distances from the bubble and spike tips to the midplane $z = 6W$, a_1 and a_2 are the fitting coefficients, γ is the growth rate. According to the classical linear theory [8,13], the growth rate γ is determined by

$$\gamma = \sqrt{A_t g k - \frac{\sigma k^3}{\rho_l + \rho_g}}. \tag{28}$$

It should be pointed out that the above formula is the theoretical result of inviscid fluids subjected to surface tension, and it is substantially difficult to give an analytical growth rate

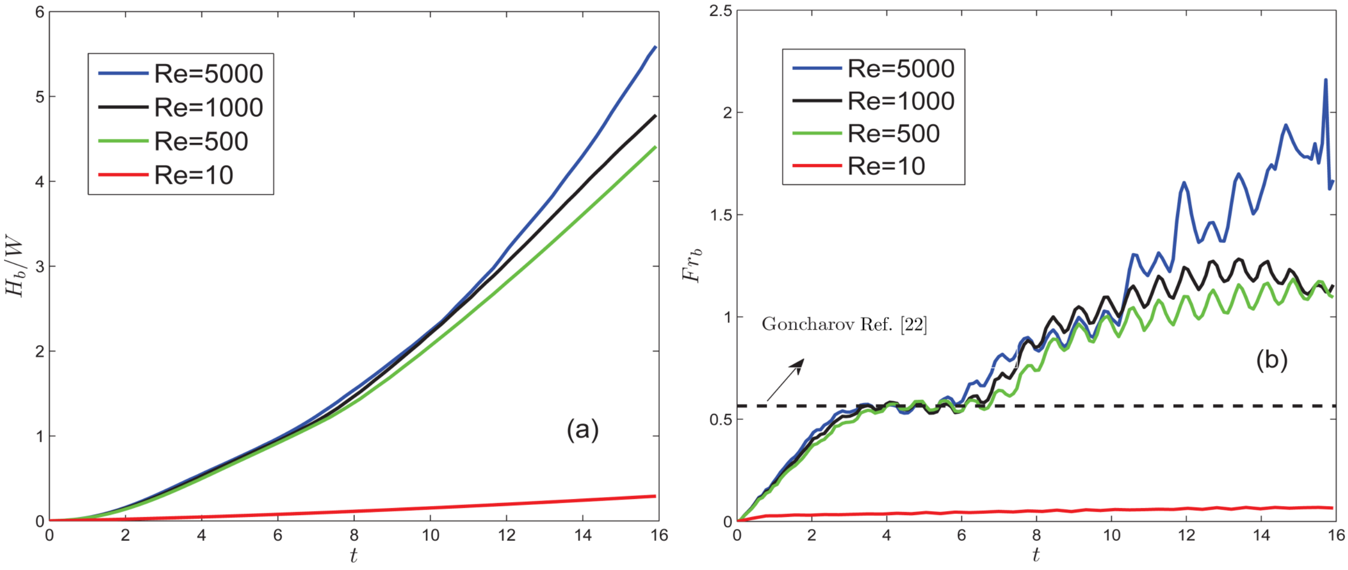

FIG. 3. Effect of Reynolds number on (a) normalized bubble amplitude and (b) normalized bubble velocity. Time is normalized by the characteristic time $1/\sqrt{A_t g k}$. The dashed line represents the analytical solution of the classic potential flow model [22].

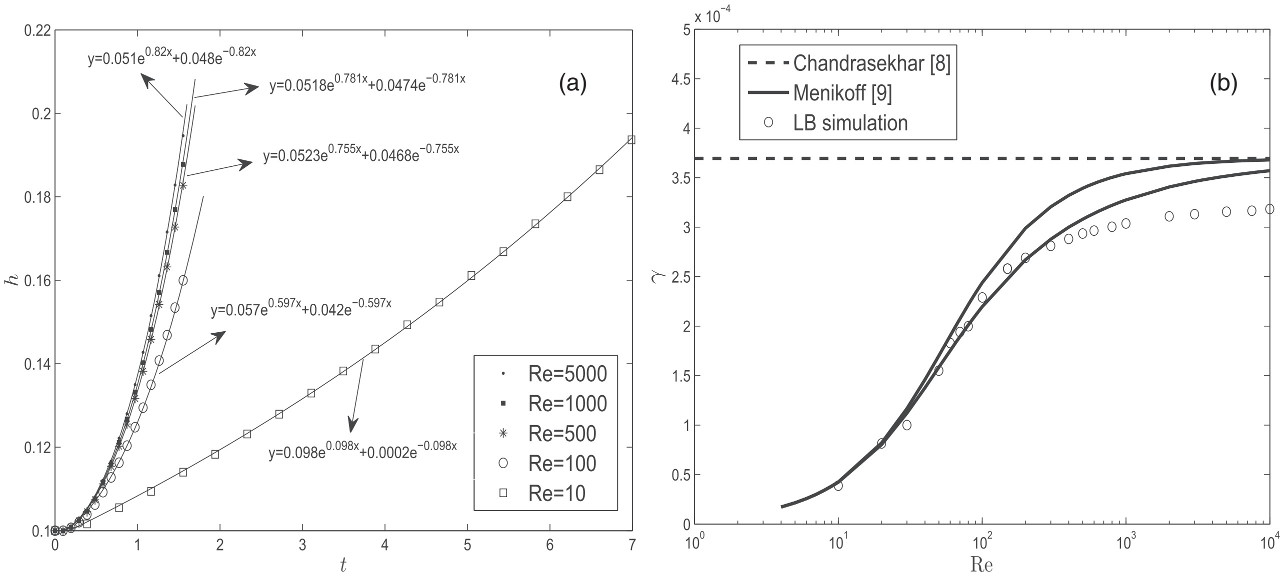

FIG. 4. (a) Time evolution of measured amplitude at linear stage for several typical Reynolds numbers. The solid lines are the fitted curves using Eq. (26) to determine the linear growth rate. (b) Dependence of the linear growth rate on Reynolds numbers.

combining the viscosity effect. Nonetheless, the lower and upper bounds to the growth rate can be presented, which satisfy the quartic and quadric equations, respectively [9],

$$\gamma_v^4 + \nu k^2 \gamma_v^3 - 2\gamma^2\gamma_v^2 - 2\nu k^2 \gamma^2 \gamma_v + \gamma^4 = 0, \tag{29}$$

$$\gamma_v^2 + 2\nu k^2 \gamma_v - \gamma^2 = 0, \tag{30}$$

where γ is the growth rate for inviscid fluids given in Eq. (28). From Eq. (30), one can easily obtain the upper bound γ_u,

$$\gamma_u = -\nu k^2 + \sqrt{\nu^2 k^4 + \gamma^2}, \tag{31}$$

and the lower bound is a real solution of Eq. (29), which should be smaller than γ_u. Figure 4(a) shows the fitted curves of the early-time amplitude at various Reynolds numbers, which can be used to determine the growth rate. It is observed from Fig. 4(a) that the numerical amplitudes fit well with the theoretical results given by Eq. (27). From Fig. 4(a) we can also measure the growth rates at different Reynolds numbers and present the results in Fig. 4(b) together with the classical growth rate and the theoretical bounds. It is seen from Fig. 4(b) that the upper bound is close to the classical result at sufficiently large Reynolds numbers, while it diverges from the classical value when Re is decreased. This discrepancy is attributed to the increasing viscosity effect that the classical linear theory fails to predict the growth rate of the viscous fluids. It is also seen from Fig. 4(b) that the present LB model can accurately predict the growth rates at low Re, which are located in the region between the lower and upper bounds. While the deviation between the numerical predictions and the theoretical bounds can be clearly observed for moderate or high Re. The reason for this disagreement has not been well understood and needs to be further studied in future work. Following the linear growth stage, the bubble evolves with a constant velocity, which suggests that the instability has entered into the second stage of the terminal velocity ($2 < t \leqslant 6$). Goncharov analytically predicted the constant bubble and spike velocities using the classic potential flow model [22],

$$u_b = \sqrt{\frac{2A_t g}{k(1+A_t)}}, \quad u_s = \sqrt{\frac{2A_t g}{k(1-A_t)}}. \tag{32}$$

Then according to Eq. (25), they yield a Fr_b of 0.564 and a Fr_s of 0.656. It should be noted that the above formulas are derived by using a cylindrical mode with the Bessel function. However, the 3D simulations of Hecht *et al.* [28] shows that the similar amplitudes can be obtained for square and cylindrical modes within machine accuracy. Therefore our present results for a square mode are valid for a flow initialized with a cylindrical mode. We compared the simulation results Fr_b and Fr_s with the corresponding theoretical values of the potential flow in Figs. 3(b) and 5(b). It can be found that a good agreement between them can be achieved. Using a similar analysis, Betti *et al.* [60] modified the classic potential flow model and gave the analytical bubble velocity including the effect of the vorticity (ϖ_0),

$$u_b = \sqrt{\frac{2A_t g}{k(1+A_t)} + \frac{1-A_t}{1+A_t}\frac{\varpi_0^2}{4k^2}}, \tag{33}$$

which results in the following Fr_b:

$$\mathrm{Fr}_b = \sqrt{\frac{2A_t g}{k(1+A_t)} + \frac{1-A_t}{1+A_t}\frac{\varpi_0^2}{4k^2}} \Bigg/ \sqrt{\frac{A_t g W}{1+A_t}}. \tag{34}$$

Note that the fluids are still assumed to be inviscid in Refs. [22,60], where the viscosity effect cannot be considered. Banerjee *et al.* [61] realized this problem and modified the terminal Fr_b including the viscosity effect,

$$\mathrm{Fr}_b = \left[\sqrt{\frac{2A_t g}{k(1+A_t)} + \frac{1-A_t}{1+A_t}\frac{\varpi_0^2}{4k^2} + k^2\nu^2} - k\nu\right] \Bigg/ \sqrt{\frac{A_t g W}{1+A_t}}. \tag{35}$$

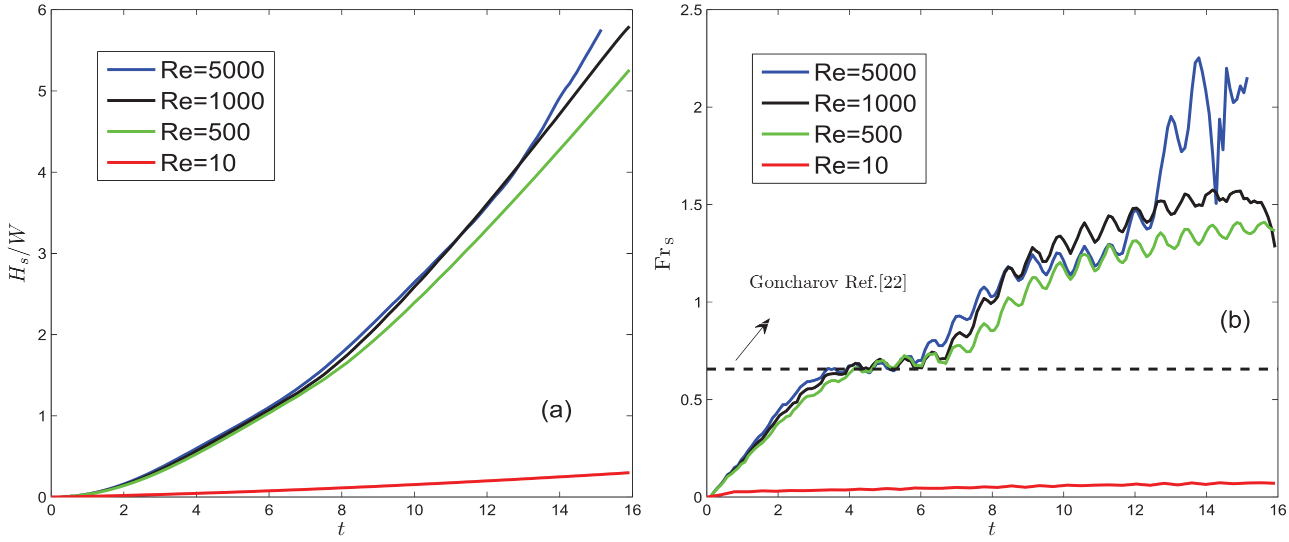

FIG. 5. Effect of Reynolds number on (a) normalized spike amplitude and (b) normalized spike velocity. Time is normalized by the characteristic time $1/\sqrt{A_t g k}$. The dashed line represents the analytical solution of the classic potential flow model [22].

Sohn [62] recently analyzed the effects of both the fluid viscosity and the surface tension on the terminal bubble velocity, and found that they could decrease the asymptotic bubble velocity. Combining these effects, the terminal Fr$_b$ can be expressed as

$$\mathrm{Fr}_b = \left[\sqrt{\frac{2A_t g}{k(1+A_t)} - \frac{3k\sigma}{16\rho_l} + k^2\nu^2} - k\nu\right] \Bigg/ \sqrt{\frac{A_t g W}{1+A_t}}. \tag{36}$$

A comparison of the terminal Fr$_b$ obtained by the present LB simulations and the above theoretical models under different Reynolds numbers is shown in Fig. 6, where the numerical predictions take the average values of the bubble Froude numbers at the second stage. Note that ϖ_0 in the formulas (33) and (34) is determined by time average of ϖ_t at the second stage, and ϖ_t is the averaging vorticity in the diagonal half-plane with vertical extent $\sim W$ behind the bubble front at time t. From Fig. 6, we can observe that for high-Re case, there is no significant difference between these theoretical models, and the computed Fr$_b$ by the LB method matches well with the corresponding analytical solutions. However, when Re is decreased, the classical potential model [22] and modification of Betti *et al.* [60] fail to predict the terminal Fr$_b$ due to the neglect of fluid viscosity effect, while it can be well described by the analytical models including the viscosity effect [61,62], and the present numerical results are also consistent with the solutions of these models. At the third stage ($6 < t \leqslant 10$), the vortical interactions gradually increase and begin to affect the velocities at the bubble and spike tips. As shown in Figs. 3(b) and 5(b), the bubble and spike are accelerated such that the velocities at the tips diverge from the solutions of the classical potential flow model. This stage is termed as reacceleration, which is first found in the 2D simulation of Glimm *et al.* [33] and further verified in 3D simulation of Ramaprabhu *et al.* [23]. Recently, the reacceleration stage of RTI was also observed by Wei *et al.* [24] using 2D direct numerical simulations and Liang *et al.* [37] using the improved 2D LB method. The reacceleration stage cannot last indefinitely. After $t > 10$, the bubble and spike Froude numbers become unstable and begin to fluctuate with the time, which suggests that the evolution of 3D RTI has transformed to the chaotic stage. Here we only focus on the bubble late-time evolution similar to 2D works [24,37]. To determine the nature of the bubble growth at late time, we measure the bubble acceleration and present the results in Fig. 7. From Fig. 7, we can observe that the normalized acceleration at late time fluctuates around a constant value of 0.16, which indicates that 3D RTI undergoes a mean quadric growth. It is noted that the bubble acceleration is also unstable during $6 < t \leqslant 10$. However, this duration is still deemed as the reacceleration stage since the bubble accelerations are always positive when they are measured with the interval of 1250 time steps. As Re is reduced gradually, the later instability stages, such as chaotic development and reacceleration, are

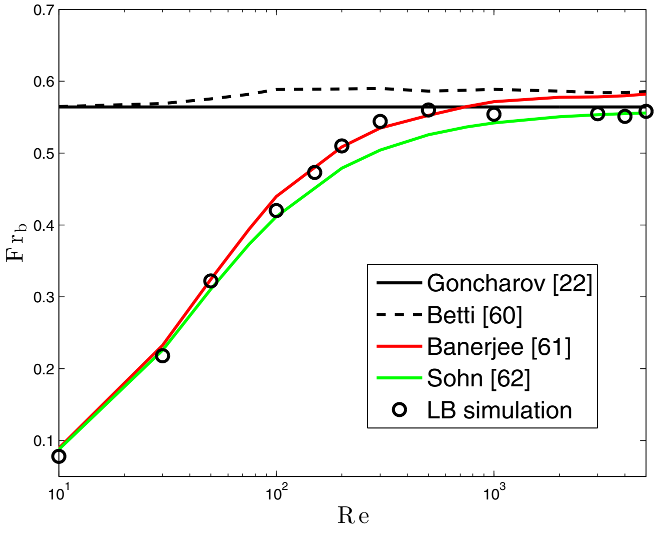

FIG. 6. A comparison of the terminal Fr$_b$ obtained by the present LB simulations and existing theoretical models under different Reynolds numbers.

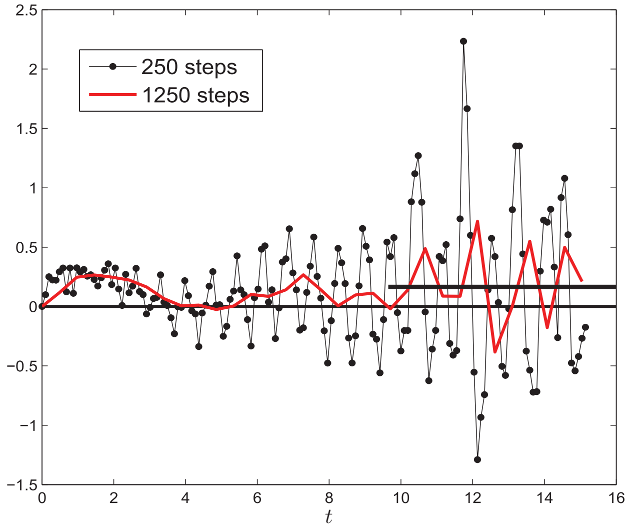

FIG. 7. Normalized bubble acceleration at high Re. Time is normalized by the characteristic time $1/\sqrt{A_tgk}$. The solid line represents a constant value of 0.16.

subsequently no longer attained. For instance, at Re = 10 the bubble and spike Froude numbers at late time approach the corresponding constant values, as shown in Figs. 3(b) and 5(b). So the late-time flow at the bubble tip is approximately described by a potential flow approach, and both the chaotic development and reacceleration stage do not appear.

B. A comparison between present results and experimental work

In this part, a comparison between our present results and the experiments of Wilkinson and Jacobs [14] is conducted. In their experiments, the Atwood number is fixed to be 0.15, which is the same as that in our numerical simulation. It is found that in our numerical results, the heavy fluid and the light one penetrate into each other, and two pairs of counter-rotating vortices are formed at the early stage. The above behaviors of the interface are qualitatively consistent with the experimental results presented in Fig. 6 of Ref. [14], where the two-layer roll-up phenomenon is also observed. We further present the bubble and spike Froude numbers as functions of the dimensionless bubble and spike amplitudes in Figs. 8(a) and 8(b), respectively, where the marked symbols were taken from experimental measurements. As can be seen from these figures, the experimental study is limited to the former three development stages of RTI, and the late stage of the chaotic development is not reached. In addition, a good agreement between our numerical results and the experimental data is also observed.

IV. SUMMARY

In this paper, we have adopted the improved lattice Boltzmann method to study the late-time 3D single-mode RTI of immiscible two-phase fluids, in which the effect of Re is examined systematically. It can be found that the instability shows distinct interfacial dynamics at different values of Re. For high Re, the instability undergoes the full range of development stages, including linear growth, terminal velocity growth, reacceleration, and chaotic development. At the linear stage, the linear growth rate was found to be lower than the theoretical bounds. In the following stage, we can observe the two-layer roll-up phenomenon, which is different from that of 2D simulation. It is also observed that the computed Fr_b and Fr_s match the analytical predictions of the classical potential flow model closely. And at the third stage, the bubble and spike tips are accelerated due to the increasing vortical interactions such that their velocities exceed the classical values. Finally, at late time, the interface undergoes the multiple-layer roll-ups, large deformation, or even chaotic breakup, which results in the formation of a very complex topology structure, and some tiny dissociative drops are also observed in the system. We further measured the bubble acceleration to show the nature

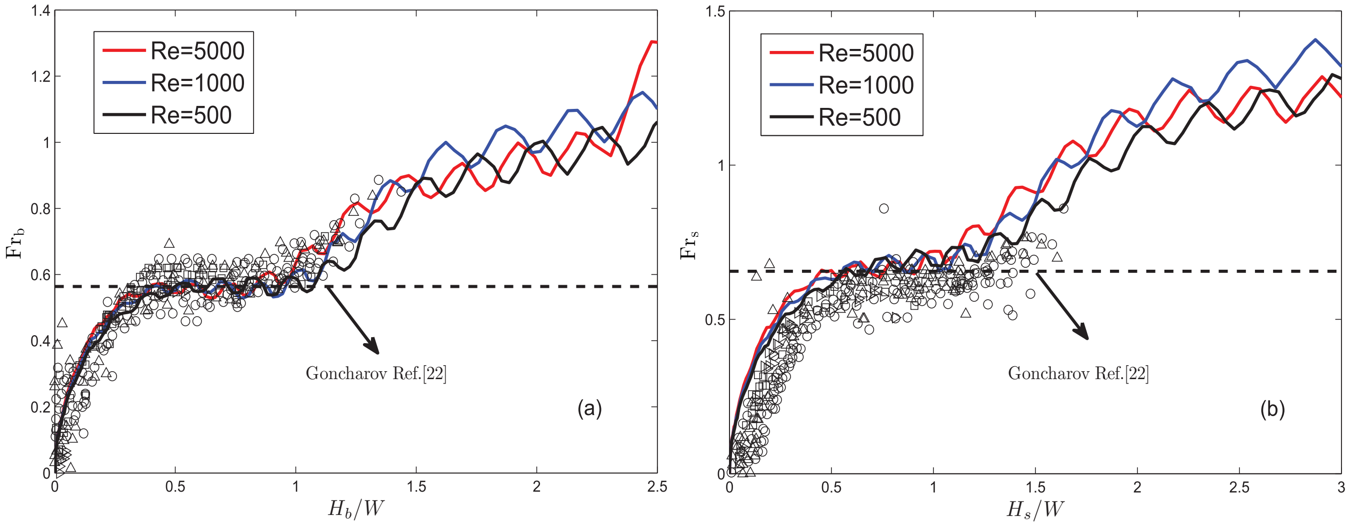

FIG. 8. Bubble (a) and spike (b) Froude numbers against dimensionless bubble and spike amplitudes, respectively. Symbols are measured from the drop tank experiments of Wilkinson and Jacobs [14], while the dashed line represents the analytical solution of the classic potential flow model [22].

of the late-time growth, and it is found that the average dimensionless acceleration is about 0.16, which indicates a mean quadratic growth. For low Re, some later development stages cannot be reached in succession. The interface becomes relatively smoothed and no breakup phenomena can be observed.

We now give a discussion on the differences between 2D and 3D results of single-mode RTI, which can be summarized as follows. First, two-layer roll-up phenomena can be observed at the early stage of 3D RTI, which is different from the 2D result that only one pair of counter-rotating vortices is found. Second, the bubble and spike fronts of 3D instability move faster than those of a 2D situation, for example, the bubble Froude number of 3D instability at the second stage closes to a constant value of 0.564, which is larger than 0.365 of the 2D case. The similar result was also reported in some previous studies [22,26]. Third, it is observed that both 2D and 3D RTI undergo mean quadratic growth at the late time, but with different paces. The growth coefficient of 3D RTI is about 0.16, while it is 0.07 in our previous 2D simulations [37]. At last, we believe that our present results would provide a more comprehensive understanding on the phenomena of bubble and spike dynamics and the behavior of the RTI.

ACKNOWLEDGMENTS

This work is financially supported by the National Natural Science Foundation of China (Grants No. 11272132, No. 51576079, and No. 51306133), and the Natural Science Foundation of Hubei Province (Grant No. 2015CFB440).

[1] B. A. Remington, R. P. Drake, and D. D. Ryutov, Rev. Mod. Phys. **78**, 755 (2006).
[2] J. A. Whitehead and D. S. Luther, J. Geophys. Res. **80**, 705 (1975).
[3] J. D. Lindl *et al.*, Phys. Plasmas **11**, 339 (2004).
[4] L. Rayleigh, Proc. London Math. Soc. **14**, 170 (1883); G. I. Taylor, Proc. R. Soc. London **201**, 192 (1950).
[5] R. Bellman and R. H. Pennington, Q. Appl. Math. **12**, 151 (1954).
[6] S. Chandrasekhar, Proc. Cambridge Philos. Soc. **51**, 162 (1955).
[7] M. Mitchner and R. K. M. Landshoff, Phys. Fluids **7**, 862 (1964).
[8] S. Chandrasekhar, *Hydrodynamic and Hydromagnetic Stability* (Oxford University Press, Oxford, 1961).
[9] R. Menikoff, R. C. Mjolsness, D. H. Sharp, and C. Zemach, Phys. Fluids **20**, 2000 (1977).
[10] D. J. Lewis, Proc. R. Soc. London, Ser. A **202**, 81 (1950).
[11] D. H. Sharp, Physica D **12**, 3 (1984).
[12] H. W. Emmons, C. T. Chang, and B. C. Watson, J. Fluid Mech. **7**, 177 (1960).
[13] J. T. Waddell, C. E. Niederhaus, and J. W. Jacobs, Phys. Fluids **13**, 1263 (2001).
[14] J. P. Wilkinson and J. W. Jacobs, Phys. Fluids **19**, 124102 (2007).
[15] J. White, J. Oakley, M. Anderson, and R. Bonazza, Phys. Rev. E **81**, 026303 (2010).
[16] M.-C. Renoult, R. G. Petschek, C. Rosenblatt, and P. Carles, Exp. Fluids **51**, 1073 (2011).
[17] S. B. Dalziel, P. F. Linden, and D. L. Youngs, J. Fluid Mech. **399**, 1 (1999).
[18] G. Dimonte and M. Schneider, Phys. Fluids **12**, 304 (2000).
[19] P. Ramaprabhu and M. J. Andrews, J. Fluid Mech. **502**, 233 (2004).
[20] G. Dimonte, Phys. Rev. E **69**, 056305 (2004).
[21] D. Oron, L. Arazi, D. Kartoon, A. Rikanati, U. Alon, and D. Shvarts, Phys. Plasmas **8**, 2883 (2001).
[22] V. N. Goncharov, Phys. Rev. Lett. **88**, 134502 (2002).
[23] P. Ramaprabhu, G. Dimonte, Y. N. Young, A. C. Calder, and B. Fryxell, Phys. Rev. E **74**, 066308 (2006).
[24] T. Wei and D. Livescu, Phys. Rev. E **86**, 046405 (2012).
[25] G. Tryggvason, J. Comput. Phys. **75**, 253 (1988).
[26] G. Tryggvason and S. O. Unverdi, Phys. Fluids A **2**, 656 (1990).
[27] X. L. Li, Phys. Fluids A **5**, 1904 (1993).
[28] J. Hecht, D. Ofer, U. Alon, D. Shvarts, S. A. Orszag, and R. L. McCrory, Laser Part. Beams **13**, 423 (1995).
[29] X. L. Li, B. X. Jin, and J. Glimm, J. Comput. Phys. **126**, 343 (1996).
[30] X. He, S. Chen, and R. Zhang, J. Comput. Phys. **152**, 642 (1999).
[31] X. He, R. Zhang, S. Chen, and G. D. Doolen, Phys. Fluids **11**, 1143 (1999).
[32] J. L. Guermond and L. Quartapelle, J. Comput. Phys. **165**, 167 (2000).
[33] J. Glimm, X. L. Li, and An-Der Lin, Acta Math. Appl. Sin. **18**, 1 (2002).
[34] A. Celani, A. Mazzino, P. M. Ginanneschi, and L. Vozella, J. Fluid Mech. **622**, 115 (2009).
[35] P. Ramaprabhu *et al.*, Phys. Fluids **24**, 074107 (2012).
[36] M. S. Shadloo, A. Zainali, and M. Yildiz, Comput. Mech. **51**, 699 (2013).
[37] H. Liang, B. C. Shi, Z. L. Guo, and Z. H. Chai, Phys. Rev. E **89**, 053320 (2014).
[38] Z. L. Guo and C. Shu, *Lattice Boltzmann Method and its Applications in Engineering* (World Scientific, Singapore, 2013).
[39] A. K. Gunstensen, D. H. Rothman, S. Zaleski, and G. Zanetti, Phys. Rev. A **43**, 4320 (1991).
[40] X. Shan and H. Chen, Phys. Rev. E **47**, 1815 (1993).
[41] M. R. Swift, W. R. Osborn, and J. M. Yeomans, Phys. Rev. Lett. **75**, 830 (1995).
[42] H. W. Zheng, C. Shu, and Y. T. Chew, Phys. Rev. E **72**, 056705 (2005).
[43] T. Lee and L. Liu, J. Comput. Phys. **229**, 8045 (2010).
[44] L. Zheng, S. Zheng, and Q. Zhai, Phys. Rev. E **91**, 013309 (2015).
[45] Y. Q. Zu and S. He, Phys. Rev. E **87**, 043301 (2013).
[46] J. W. Cahn and J. E. Hilliard, J. Chem. Phys. **28**, 258 (1958).
[47] P. Lallemand and L. S. Luo, Phys. Rev. E **61**, 6546 (2000).
[48] Z. H. Chai, B. C. Shi, Z. L. Guo, and J. H. Lu, Commun. Comput. Phys. **8**, 1052 (2010).
[49] M. E. McCracken and J. Abraham, Phys. Rev. E **71**, 036701 (2005).
[50] H. Liang, B. C. Shi, and Z. H. Chai, arXiv:1507.07294 [physics.comp-ph].
[51] H. Liang, Z. H. Chai, B. C. Shi, Z. L. Guo, and T. Zhang, Phys. Rev. E **90**, 063311 (2014).

[52] D. Jacqmin, J. Comput. Phys. **155**, 96 (1999).
[53] H. Yoshida and M. Nagaoka, J. Comput. Phys. **229**, 7774 (2010).
[54] Z. L. Guo and C. G. Zheng, Int. J. Comput. Fluid Dyna. **22**, 465 (2008).
[55] D. d'Humieres, I. Ginzburg, M. Krafczyk, P. Lallemand, and L. S. Luo, Phil. Trans. R. Soc. Lond. A **360**, 437 (2002).
[56] Q. Li, K. H. Luo, Y. J. Gao, and Y. L. He, Phys. Rev. E **85**, 026704 (2012).
[57] B. C. Shi and Z. L. Guo, Phys. Rev. E **79**, 016701 (2009).
[58] Q. Lou, Z. L. Guo, and B. C. Shi, Europhys. Lett. **99**, 64005 (2012).
[59] K. N. Premnath and J. Abraham, J. Comput. Phys. **224**, 539 (2007).
[60] R. Betti and J. Sanz, Phys. Rev. Lett. **97**, 205002 (2006).
[61] R. Banerjee, L. Mandal, S. Roy, M. Khan, and M. R. Guptae, Phys. Plasmas **18**, 022109 (2011).
[62] S.-I. Sohn, Phys. Rev. E **80**, 055302(R) (2009).